Micro Fluid Jet Polishing

Anthony T. Beaucamp*

*Dept. of Micro-Engineering, Kyoto University, Kyoto, Japan

Abstract

Micro fluid jet polishing (MFJP) is a super-fine machining process in which a slurry of loose abrasives and carrier fluid is pressurized and pushed out through a nozzle orifice, generating a fluid beam of small diameter. Impingement of the beam onto a workpiece surface results in a sub-millimeter footprint of time dependent material removal. The relatively benign processing pressure and abrasive grain size in MFJP, as compared to micro waterjet machining, assures a low material removal rate that promotes smoothing of the workpiece surface. In this chapter, the basic principles and applications of the MFJP process are first reviewed. Characterization of the process parameters, their typical value ranges, and best practice in implementing the MFJP process are discussed, together with an in-depth analysis of the process mechanism including: jet plume formation, abrasive particles entrainment, material removal by particle impacts, and surface integrity considerations when using MFJP on hard and brittle materials. The basic principles of deterministic finishing by MFJP are discussed next, whereby a workpiece shape accuracy may be improved through iterative measurement and processing, with an introduction to the associated numerical methodology being provided. Finally, a number of enhancements to the MFJP process are considered, including: submerged, air-assisted, ultrasonic-cavitation assisted, non-Newtonian and magnetorheological fluid assisted MFJP, as well as multi-jet designs of the nozzle cavity. Useful indicators are provided, as to the advantages and shortcomings of such enhancements.

X.1 Introduction

X.1.1 Principle of MFJP Process

Micro fluid jet polishing (MFJP) is used to refer to a class of material processing technologies in which loose abrasives (such as diamond or alumina) and a carrier fluid (typically water) are pre-mixed into a slurry, that is pressurized and pumped into a nozzle cavity which it then escapes through a small cylindrical outlet [Faehnle 1998], as shown in Fig. X-1(a). The resulting fluid jet beam impinges the workpiece surface either perpendicularly or at a deflection angle, allowing individual abrasive particles entrained within the carrier fluid to impact the workpiece material, as shown in Fig. X-1(b). The full or even partial release of the abrasives kinetic energy results in removal of material from the workpiece surface without the need for a pad or cloth, as is typical in conventional polishing.

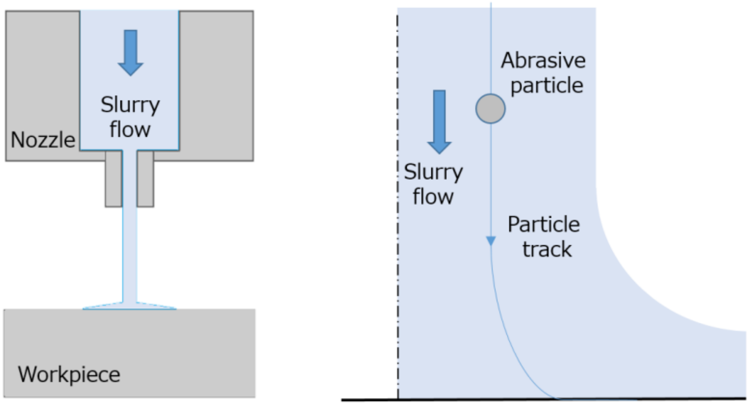

(a) Configuration of nozzle (b) Trajectory of abrasives

Fig. X-1. Principle of micro fluid jet polishing (MFJP)

Some advantages of the MFJP process include the possibility of generating sub-millimeter diameter footprints of ductile mode material removal, as well as the ability to maneuver the thin beam of slurry around difficult areas such as bore holes, steeply concave surfaces, deeply recessed areas, and workpiece corners. Tool wear issues are usually limited to the slow and progressive breakdown of abrasive particles, which can be predictively controlled by using abrasives of adequate hardness as compared to the workpiece material. Furthermore, the excellent stability of material removal rate achievable under well-controlled conditions (see section X.2) allows for usage of MFJP as a deterministic finishing process. Corrective polishing of optical surfaces to a geometrical shape accuracy less than 100 nm Peak-to-Valley (P-V) is routinely attainable, through variable feed scanning of the workpiece with the slurry beam.

X.1.2 Some Applications of MFJP

X.1.2.1 Polishing of Micro-Lens Molds

Fabrication of optical quality micro-lens molds and mold arrays is a key technological enabler for a number of industrial sectors, such as consumer cameras and smartphones, endoscopes, and fiber optics end-connectors to communication terminals. Single lens optical designs usually rely on the use of aspheric surfaces, for correction of spherical aberrations. Such aspheric shapes may be generated by diamond turning or micro-grinding of materials such as electroless nickel or nickel alloys (for replication by plastic injection), and tungsten carbide or silicon carbide (for replication by glass injection). Post-polishing of the pre-machined surfaces is required in order to meet the stringent surface roughness (less than 2 nm Ra) and form accuracy (less than 60 nm P-V) requirements of visible light optical systems. As well as the small overall size of the optical aperture (usually less than 1-2 mm), the asphericity of the optical surface implies variations of the surface curvature that translates into surface features with a lateral resolution of few hundred microns, which are very challenging to polish with conventional compliant polishing tools. The ability to adapt the beam size to aspheric feature resolution thus makes MFJP a well-suited process for final finishing of micro-lens molds and mold arrays (Fig. X-2).

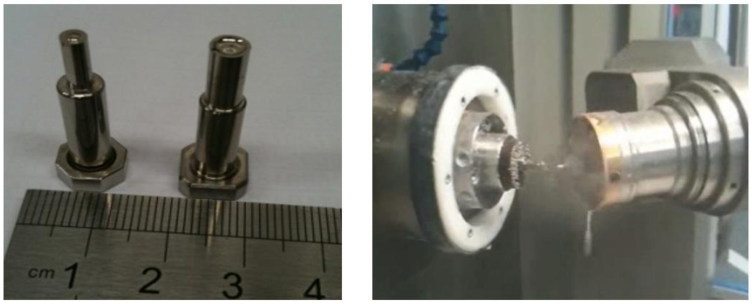

(a) Pair of aspheric micro-molds (b) Polishing of micro-mold on MFJP machine

Fig. X-2. Polishing by MFJP of nickel plated micro-molds, for replication of smartphone camera lenses

X.1.2.2 Polishing of Micro-Channels

By operating MFJP with a small nozzle outlet of few hundred microns in diameter, polishing of micro-grooves and channels is technologically possible. In the polishing of such features, it was observed that sidewalls of the grooves promote development of a stagnation effect area, which leads to higher velocity fluid flow that is aligned with the direction of the micro-structures [Matsumura 2011]. Fig. X-3 shows an example of micro-grooves, 100 µm wide and few microns deep, used for channeling of human cells on glass chips. The channels were pre-machined by micro-milling and finished by MFJP. Effective removal of milling marks and sub-surface crack damage can be clearly observed, with final surface finish of 25 nm Ra.

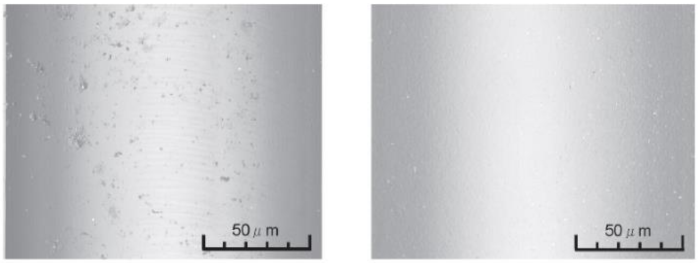

(a) Original (b) Polished

Fig. X-3. Polishing of micro-milled channels by MFJP [Matsumura 2011]

X.1.2.3 Smoothing of Micro-Cusps

The periodic structures generated by fine pre-machining processes such as diamond turning and micro-grinding are of particular interest. The fine cusping left over from these processes is typically a few microns wide, and only a few nanometers deep. Nevertheless, it can cause very noticeable degradation of the optical performance due to light diffraction and scattering; this phenomenon usually appears in the form of rainbow patterns when observing the surface at a glancing angle of incidence. Removal of such micro-cusps with compliant polishing tools can be exceedingly time consuming, as these tools have a tendency to follow the patterns rather than cut through them. By comparison, the MFJP process has a remarkable propensity for smoothing fine regular structures on such pre-machined surfaces. Fig. X-4 shows a typical example of diamond turning marks on an electroless nickel plated surface, which were completely eradicated after the removal of a few hundred nanometers of material by MFJP [Beaucamp 2013].

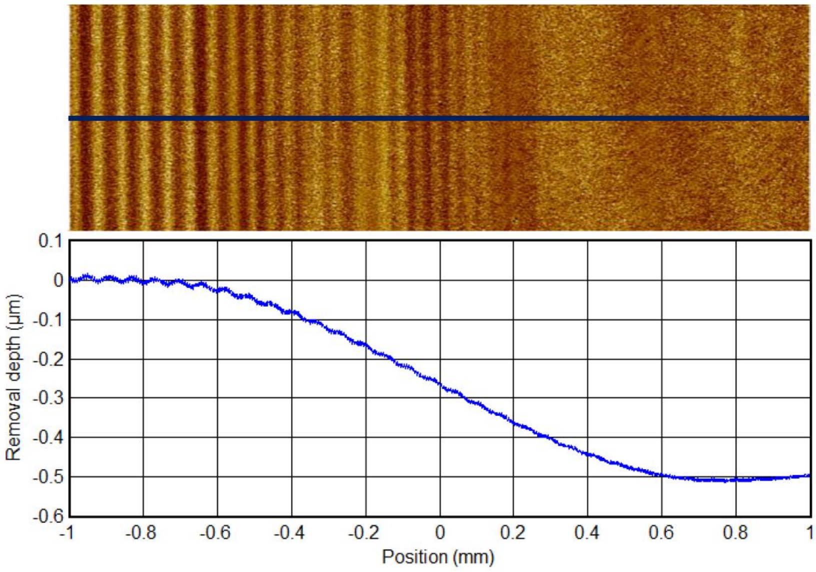

Fig. X-4. Removal of diamond turning marks on electroless nickel plating by MFJP [Beaucamp 2013]

X.1.2.4 Generation of Functional Surfaces

When operating under well-controlled conditions (see section X.2), evolution of the material removal rate in the MFJP process can become stable and predictable. It may then be employed to generate functional surfaces with regular patterns and structures that find application in micro-electromechanical systems (MEMS), micro-fluidics, and controlled lubrication of surfaces. Based on scanning of the workpiece surface with a stable footprint, moderation of the beam displacement feed results in localized variations of the material removal depth and appearance of peaks and valleys. Using numerical methods such as point spread functions (see section X.4), functional patterns with a lateral resolution half that of the footprint can be polished onto the surface. This deterministic polishing method may be used either on glass plates for direct application, or to process molding inserts made from nickel alloy or steel, from which plastic or glass plates can be replicated. Depth resolution of few nanometers, and accuracy of few dozen nanometers, can be technologically realized. Fig. X-5 shows some examples of functional patterns generated by MFJP on BK7 glass plates [Cao 2016].

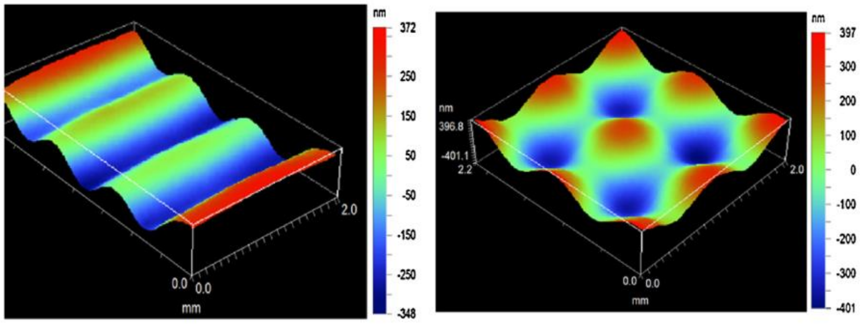

Fig. X-5. Generation of functional patterns on BK7 glass by MFJP [Cao 2016]

X.2 MFJP Process Parameters

The principal process parameters in MFJP are listed in Table X-1, together with their typical value ranges. There are three main categories: (1) nozzle parameters, (2) fluid parameters, and (3) abrasive parameters. While there exists similarities with micro waterjet machining, such as the configuration of the nozzle and pressurization of the carrier fluid, processing conditions in MFJP are much more benign in order to ensure ductile cutting of the workpiece surface rather than brittle removal of material.

Table X-1. Typical process parameters in MFJP.

Parameter Type	**Typical Values**
Nozzle parameters	
Nozzle outlet diameter	0.1 - 1.0 mm
Nozzle stand-off distance	1.0 - 20 mm
Nozzle attack angle	90°
Fluid parameters	
Carrier fluid	Water
Fluid pressure	0.2 - 2.0 MPa
Abrasive parameters	
Abrasive type	Al_2O_3, CeO_2, SiC, Diamond
Abrasive grain size	0.1 - 10 µm
Abrasive concentration	10 - 40 g/L

X.2.1 Nozzle Outlet

The nozzle outlet diameter typically ranges between 0.1 and 1.0 mm, with material removal rate increasing as a function of the squared value of this diameter (all other parameters being equal). When using smaller diameter outlets below 0.5 mm, the installation of an inline filter between the pump and nozzle cavity is recommended in order to avoid potential obstruction of the outlet. While conventionally drilled tapered stainless steel nozzles may be employed, the best practice is to use laser drilled sapphire or diamond inserts, as these are machined with a higher degree of precision that results in noticeably narrower and more rotationally symmetric removal footprints, as shown in Fig. X-6.

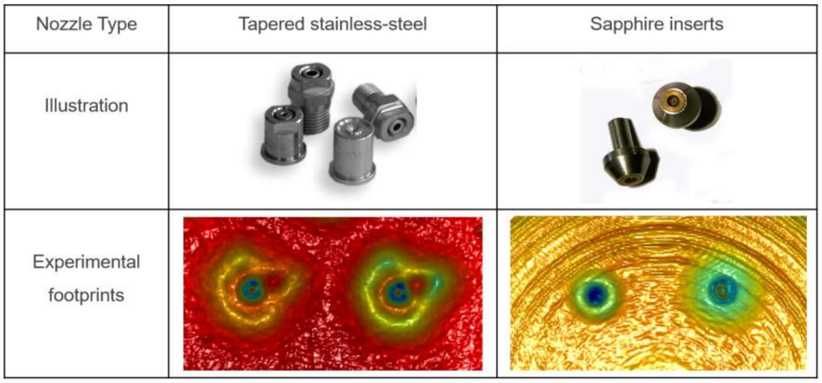

Fig. X-6. Experimental comparison of MFJP footprints generated with tapered stainless steel vs. sapphire insert nozzle types.

A further advantage in using laser drilled inserts is the superlative sharpness of the bore edges, which promotes a strongly negative pressure gradient as the carrier fluid flows around the inner edge of the outlet. For inlet pressure more than around 0.4 MPa, fluid depressurization at this edge results in cavitation that leads to the development of a vena contracta region on the outlet wall close to this inner edge, as shown in Fig. X-7. As fluid flows around the vena contracta, it temporarily detaches from the outlet wall. Under increased inlet pressure more than around 0.6 MPa, detachment of the carrier fluid reaches across the entire length of the nozzle outlet wall, thanks to a continuous layer of vaporized fluid. This condition, known as a hydraulic flip, brings two key advantages to the MFJP process: (1) narrowing of the fluid jet beam that offers enhanced processing resolution, and (2) greatly enhanced longevity of the insert as abrasive particles seldom come into contact with the nozzle outlet wall.

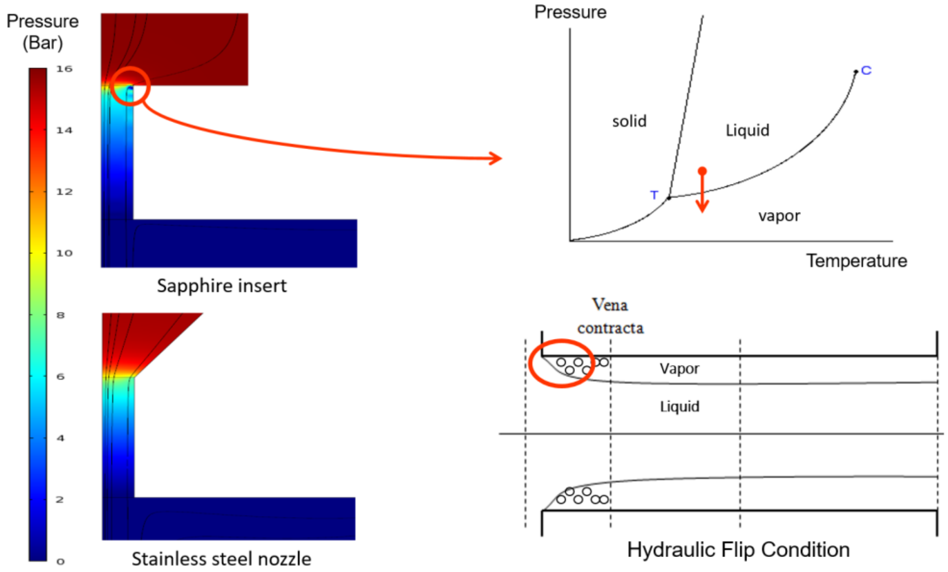

Fig. X-7. Simulation of pressure field difference between sapphire and tapered stainless steel nozzle outlet, and the resulting development of hydraulic flip condition in the case of sapphire inserts.

X.2.2 Fluid Pressurization

Pressurization of the MFJP slurry at the nozzle inlet between 0.2 and 2.0 MPa is the typically recommended range, as it allows lower impact energy of the abrasive particles when compared to micro waterjet machining, ensuring that brittle damage does not occur on the workpiece surface. Special care and attention should be paid when designing the fluid pressurization system, as oscillations of nozzle inlet pressure inevitably translates into oscillations of the material removal rate at the workpiece surface. Fig. X-8 shows a typical setup designed to reduce such nozzle inlet pressure oscillations [Beaucamp 2012]: In order to maximize efficiency of the pressurization system, a low pressure pump acts as a fluid mixer (to keep abrasive particles in suspension) and feed-in to a high pressure pump. The high pressure pump may be of the plunger, diaphragm or Archimedean screw type, with the latter usually preferred as it operates with lesser oscillations of the fluid pressure.

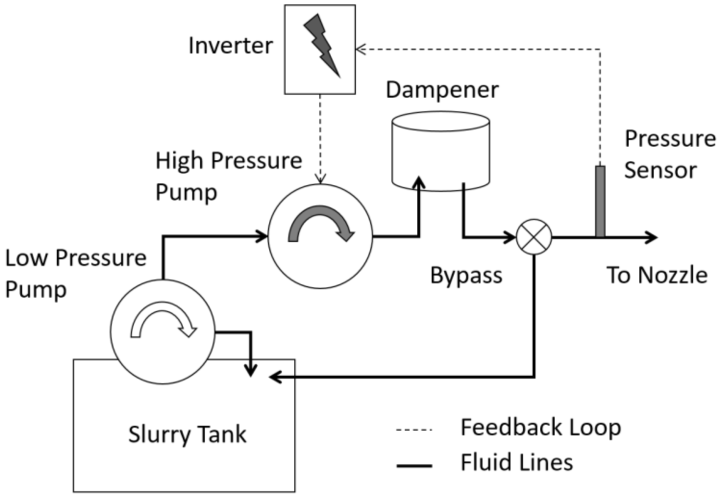

Fig. X-8. Typical implementation of feedback enabled fluid pressurization system in MFJP [Beaucamp 2012]

The pressurized fluid then flows through a dampener in order to reduce residual oscillations, after which it enters a variable bypass that allows a fraction of the fluid through to the nozzle inlet, while the rest flows back to the slurry tank. The bypass is useful for steering operation of the system towards high revolution of the pump, as high frequency pressure oscillations are more effectively absorbed by the dampener. A pressure sensor is located between the bypass and nozzle inlet, and connects to a control system that monitors fluid pressure and corrects residual fluctuations by feeding back to the inverter powering the high pressure pump, as well as regulating the opening level of the bypass. The usefulness of this kind of advanced system, capable of pressure monitoring and feedback loop, has been demonstrated in the case of optical glass polishing [Beaucamp 2012], with reduction in surface waviness from 16 nm down to 1.5 nm rms when the feedback loop is enabled.

X.2.3 Abrasive Particles

Typical abrasive particle size ranges between 0.1 and 10.0 µm. The selection of abrasive particle type depends mostly on the workpiece material, with typical recommendations as follows: Al_2O_3 for metals such as nickel and steel, CeO_2 for optical glass, and SiC or diamond for harder materials such as ceramics and super-alloys. The influence of abrasive size and nozzle inlet pressure on the material removal rate and surface roughness has been well documented in the literature, such as in the case of optical glass [Booij 2003] and electroless nickel [Beaucamp 2013]. As shown in Fig. X-9, the material removal rate typically increases exponentially as a function of both inlet pressure and abrasive particle size, while surface roughness follows a more linear relationship of these parameters. These trends make MFJP an attractive process when used in multiple stages, with a first stage of larger abrasives used for bulk material removal without excessive degradation of surface roughness, and a second stage of smaller abrasives used for final finishing of the surface.

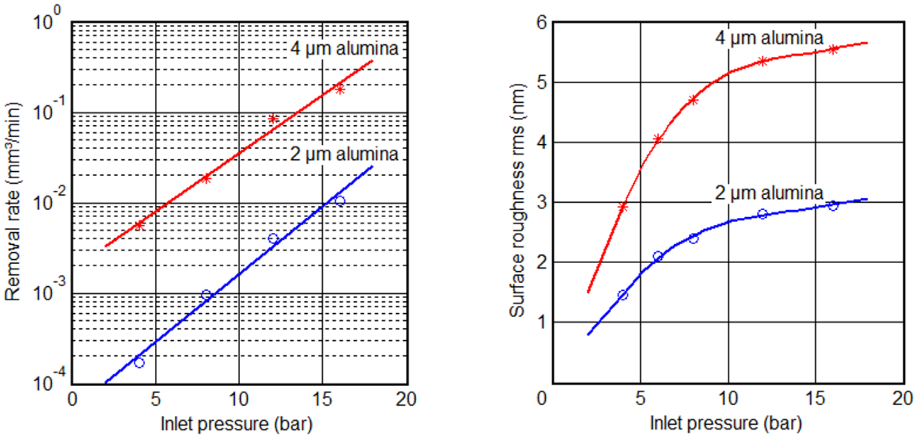

(a) Material removal rate (b) Surface roughness

Fig. X-9. Influence of abrasive size and inlet pressure on removal rate and surface roughness in MFJP [Beaucamp 2013]

Contamination of the workpiece surface by embedded abrasive particles may occur when processing by MFJP soft materials such as electroless nickel plating or nickel alloys. An example is shown in Fig. X-10, in which an electroless nickel surfaces were contaminated by embedded alumina particles [Beaucamp 2014]. Whenever such embedding occurs, it can very difficult to remove the abrasive particles from the surface (even with the use of ultrasonic vibration assisted cleaning equipment). Contamination of the surface typically increases as a function of the MFJP inlet pressure, and as the inverse function of the abrasive particle size. Thus, in cases where contamination of the surface is observed, loading the carrier fluid with a slightly larger abrasive grit size while reducing the operating pressure of the system is recommended. This remedial action will usually maintain both the removal rate and surface roughness level, while drastically reducing surface contamination by the abrasives.

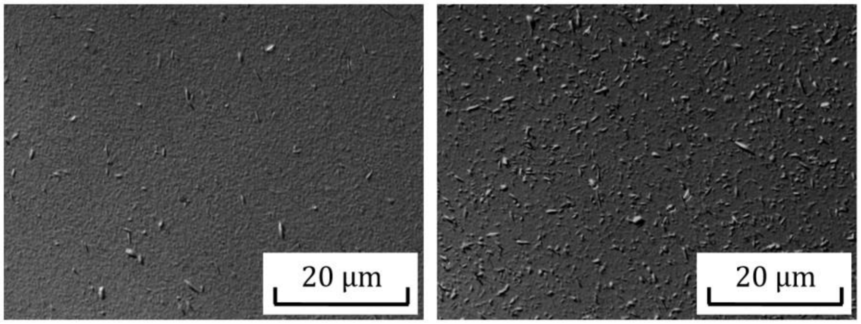

(a) Processing at 0.8 MPa (b) Processing at 1.6 MPA

Fig. X-10. Contamination of electroless nickel surfaces by embedded 2 µm alumina abrasive particles after processing by MFJP [Beaucamp 2014]

X.3 MFJP Process Mechanism

The process mechanism in MFJP can be broken down into four separate basic components: (1) development of the jet plume at the nozzle outlet and subsequent impingement of the workpiece surface, (2) entrainment of abrasive particles by the carrier fluid, (3) removal of workpiece material by abrasive particles grazing the surface, and (4) impact of the process on surface integrity when processing hard and brittle materials. Each of these components is separately detailed in the following sections.

X.3.1 Development of Jet Plume and Impingement of Workpiece

Considering that the carrier fluid is nearly incompressible at the typical operating pressure and temperature of the MFJP process, the average velocity of the jet plume at the nozzle outlet can be estimated from Bernoulli's equation:

$$\mathrm{P} = \frac{1}{2}\rho \mathrm{v}^2 \tag{1}$$

where P [Pa] is the inlet pressure, ρ [kg.m^{-3}] is the carrier fluid density, and v [m.s^{-1}] the fluid velocity at the nozzle outlet. For the typical operating pressure conditions of 0.2 to 2.0 MPa, nozzle outlet velocities thus range between 20 and 60 m.s^{-1}.

More detailed modelling of the jet plume formation requires application of the Navier-Stoke equations to a two-phase flow computational fluid dynamics problem. In their incompressible form, the Navier-Stokes equations are reduced to the expression:

$$\rho\left(\frac{\partial \mathrm{v}}{\partial \mathrm{t}} + \mathrm{v}.\nabla \mathrm{v}\right) = -\nabla \mathrm{P} + \mu \nabla^2 \mathrm{v} + \mathrm{F} \tag{2}$$

where μ [Pa.s] is the fluid viscosity, and F [N] represents external forces acting on the fluid. The left-side of the equation generally represent the fluid inertia, and the right side the divergence of stress and other forces. The viscosity of a slurry mixture can be calculated from the volume fraction of solid particles in the carrier fluid using the Thomas equation, which arises from a combination of Brownian motion theory and experimental observations at high particle concentrations:

$$\mu_r = 1 + 2.5\varphi + 10.05\varphi^2 + \mathrm{A}e^{\mathrm{B}\varphi} \tag{3}$$

where μ_r is the relative viscosity of the slurry to that of water, φ the volume fraction of solid particles, and $A = 0.00273$, $B = 16.6$ (empirically derived constants).

When dealing with the two-phase propagation of slurry through surrounding air, a phase function ϕ is used to describe the interface between air and carrier fluid, with fluid density and viscosity being assigned for air or slurry on either side of this interface. From an initial state ϕ_0, in which the carrier fluid fills the inside of the nozzle cavity and air occupies the outside, the interface is convected by the fluid velocity field. This evolution is described by the Cahn-Hilliard equation:

$$\frac{\partial \phi}{\partial \mathrm{t}} + (\mathrm{v}.\nabla)\phi = \nabla.\gamma\nabla \mathrm{G} \tag{4}$$

where γ [$m^3.s.kg^{-1}$] is a mobility parameter controlling the relaxation time (used to prevent oscillations of the interface and improve numerical instability), and G [Pa] is the chemical potential of the system. The left side of the equation convects the air/slurry interface, while the right side seeks to minimize the total free energy of the system. While a system of two immiscible fluids has a free energy comprised of mixing, bulk distortion and anchoring, in MFJP the problem may be simplified by retaining only the mixing energy, in which case the potential G is derived from the Ginzburg-Landau equation:

$$G = \lambda(-\nabla^2\phi + \frac{\phi(\phi^2 - 1)}{\varepsilon^2}) \tag{5}$$

where ε [m] is an arbitrary capillary width (thickness of the air/carrier fluid interface region), and λ [N] represents the mixing energy density. These two parameters are closely linked to the surface tension coefficient σ [N/m] through the expression:

$$\sigma = \frac{2\sqrt{2}}{3}\frac{\lambda}{\varepsilon} \tag{6}$$

Turbulence of the fluid flow through the outlet and near the workpiece surface requires adequate treatment by introducing turbulence model equations into the simulation. Table X-2 shows a comparison of three of the most common turbulent flow models: k-ε, k-ω, and SST. The SST model is well suited to jet plume formation and impingement problems, as it combines robustness of the k-ω model in the near wall regions (including the severe pressure gradient at the inner edge of the outlet), and numerical stability of the k-ε model in the free shear flow regions of the jet plume. A complete formulation of the SST model is readily available in the literature [Menter 1994].

Table X-2. Comparison of three turbulent flow models

Model	*k-ε*	*k-ω*	SST
Concept	2 transport equations: turbulent kinetic energy ***k*** turbulent dissipation ***ε***	2 transport equations: turbulent kinetic energy ***k*** turbulent frequency ***ω***	Combination of: ***k-ω*** in near wall regions ***k-ε*** in free stream regions
Pros/Cons	+ Numerically robust - Valid only if fully turbulent - Poor results against severe pressure gradients	+ Superior treatment of near wall regions + Suitable against severe pressure gradients - Flow separation can occur excessively in free streams	+ Well suited for laminar to turbulent flow transitions - Less suitable for free shear flow regions

Fig. X-11 shows a typical time series simulation of jet plume development and surface impingement, based on the numerical method described above [Beaucamp 2012]. After initial formation of a wide front by the fluid, which pushes out the surrounding air, the fluid stream rapidly stabilizes into a near laminar flow condition out of the nozzle. As the MFJP beam impinges the workpiece surface, a high pressure region is established at the center of the jet impact zone, with fluid thereupon flowing around this stagnation point.

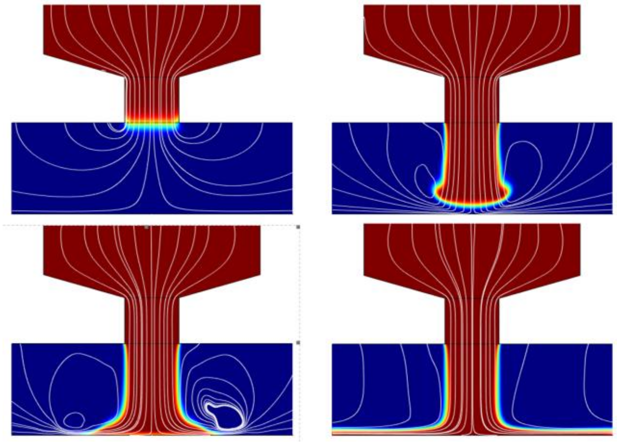

Fig. X-11. Development of MFJP jet plume and impingement of workpiece surface [Beaucamp 2012]

Additionally, edge effects may require special consideration in the case of optical surface polishing. For this type of application, geometrical distortions of the surface such as edge roll and shaving is considered as one of the more critical technical issues, which can dominate the performance of an optical system. When running 3D computational fluid dynamics simulations, it was found that fluid velocity in the edge region can increase by a factor of 2 relative to the inner region, as shown in Fig. X-12(a)(b) [Fang 2006].

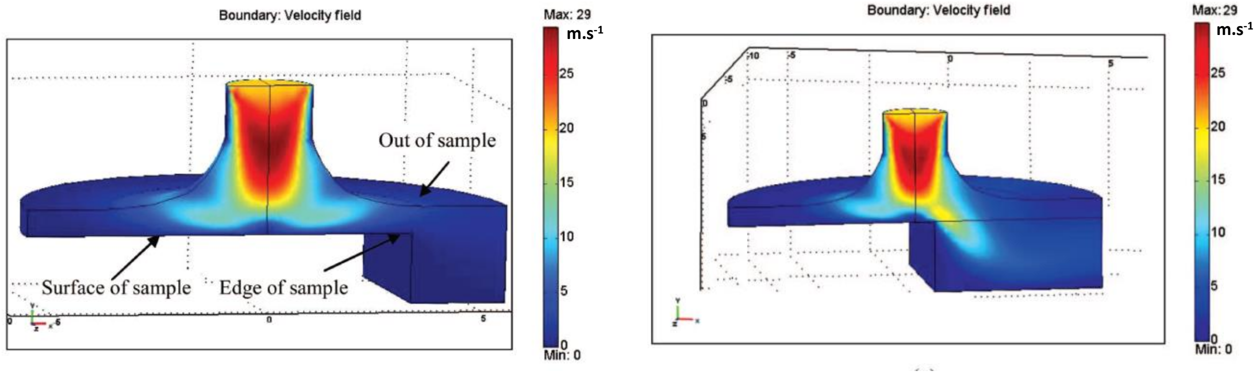

(a) Fluid velocity field in inner region of sample (b) Fluid velocity field at edge region of sample

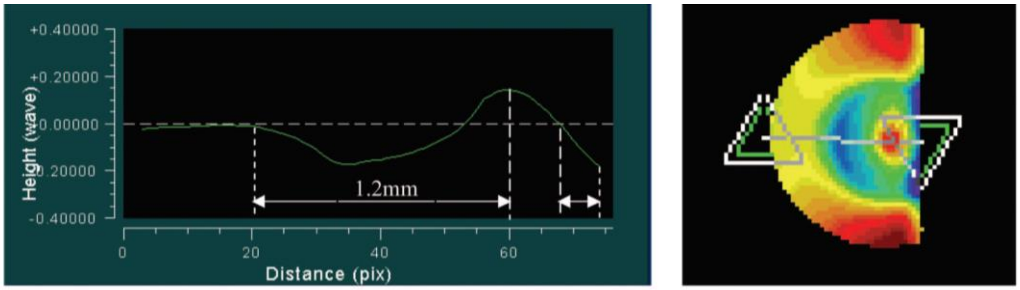

(c) Material removal profile at ragged edge of sample

Fig. X-12. Characteristics of jet plume velocity field and material removal profile, between the inner and edge regions of a planar surface [Fang 2006]

Such distortion of the fluid velocity field influences material removal at the ragged edge of the workpiece (width of approximately 0.2 mm): the usually circular influence region widens along the edge and features excessive removal of material compared with the inner region, as shown in Fig. X-12(c). The accuracy of deterministic finishing algorithms is improved when taking this effect into account (see section X.4).

X.3.2 Entrainment of Abrasive Particles by Carrier Fluid

The motion of individual abrasive particles within the carrier fluid can be derived from the application of Newton's second law of motion to the slurry mix, whereby:

$$m_p \frac{\partial^2 \mathrm{p}}{\partial \mathrm{t}^2} = \mathrm{F} \tag{7}$$

where *p(t)* is the trajectory of a single abrasive particle, m_p [kg] the abrasive particle mass, and F the sum of forces acting on the particle. External forces acting on a particle within a carrier fluid comprise gravitation, buoyancy, as well as collisions with other particles. In the case of MFJP, it is assumed that all these factors are small in comparison with the drag force issuing from the relative motions of the particle and high velocity carrier fluid. This drag force can be estimated using Rayleigh's equation:

$$\mathrm{F} = \rho \mathrm{C_D} \mathrm{v}^2 \frac{\mathrm{A}}{2} \tag{8}$$

where C_D is the drag force coefficient (relating to the shape of the particle) and A [mm^2] is the projected area of the particle relative to the fluid flow direction. Typically, abrasives follow the jet plume streamlines out of the nozzle, and only start diverging in the region close to the workpiece surface, due to their downward momentum. Fig. X-13 shows an example of simulated abrasive particle tracks near the center of the jet impingement zone [Beaucamp 2012]. The color map denotes the velocity field of the carrier fluid, while individual particle trajectories are shown as black curves and can be seen to deviate from the carrier fluid velocity field in the vicinity of the stagnation region at the center of the impact zone. From these simulations, the spatial distribution of the abrasive particles first impact point $\sigma_A(r)$ [$mm^{-2}.s^{-1}$], and their impact velocity vector $\vec{v}(r)$ can be estimated.

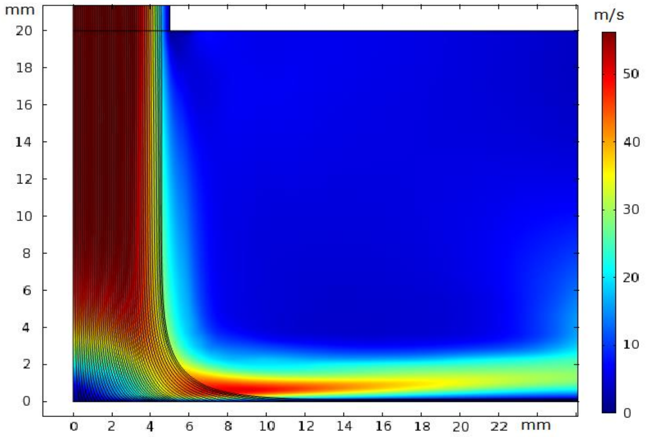

Fig. X-13. Tracks of abrasive particle trajectories through the MFJP carrier fluid stream [Beaucamp 2012]

Fig. X-14 shows examples of simulations for the spatial distribution of abrasive particles first impact on the workpiece surface, and the impact velocity. The spatial distribution $\sigma_A(r)$ is a Gaussian-shaped curve, with a small depression at center that corresponds to the increased fluid drag in the stagnation region of the impinging jet. At lower pump pressures such as 0.4 MPa, only a small number of abrasive particles actually reach the surface. The total number of particles reaching the surface increases approximately as a square law of the pump pressure for the typical operating range of the MFJP process. A similar law holds true when the abrasive grit diameter is increased. The impact velocity distribution $|\vec{v}|$ is an inverted W-shaped curve, with almost zero velocity at the center of the stagnation area, and peak velocity at a radial distance of around 2 times the nozzle outlet half-diameter.

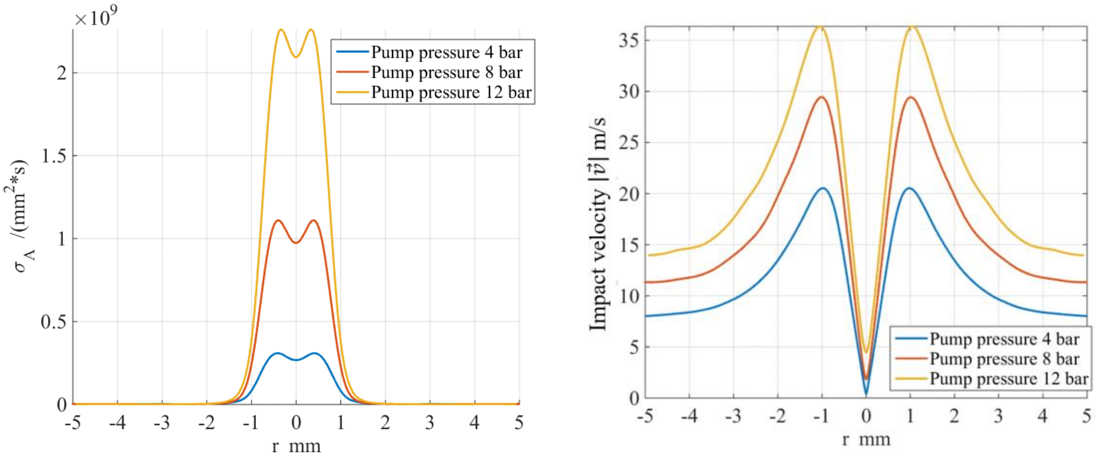

(a) Spatial distribution of abrasive particles (b) Impact velocity of abrasive particles

Fig. X-14. Simulations of MFJP abrasive particle impacts on the workpiece surface, as a function of pump pressure [Katsuura 2018]

Experimental observation of abrasive particle tracks through the impact zone of the MFJP beam is possible through the use of particle image velocimetry (PIV). Abrasive particles can be coated with a fluorescent dye, which is activated by laser illumination of the fluid flow area captured by a high speed camera. Fig. X-15 shows an example of CeO2 particles coated with such fluorescent dye, and Fig. X-16 shows a snapshot of the particles moving through an illuminated area close to the workpiece surface [Wager 2005]. Experimental data for the particle trajectories has been found to agree reasonably well with predictions from computational fluid dynamics models.

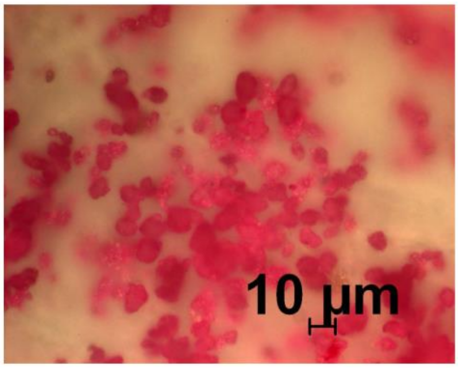

Fig. X-15. Cerium oxide particles coated with fluorescent die [Wager 2005]

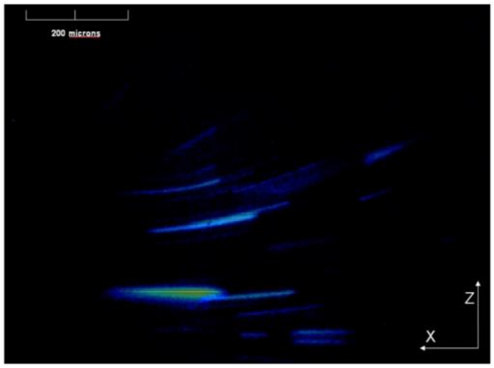

Fig. X-16. Snapshot of abrasive particles motion close to the workpiece surface [Wager 2005]

X.3.3 Material Removal by Abrasive Impacts

Modelling of material removal in abrasive waterjet cutting usually takes into account particle rotation due to the violent mixing of fluid and abrasives in the nozzle cavity, with particle rotation direction influencing the formation of chips on the workpiece surface. However, since the carrier fluid and abrasive particles in MFJP are pre-mixed inside a slurry tank, the influence of particle rotation energy can be considered to be negligible when abrasives impact the surface. The impact velocity of abrasive particles on the workpiece surface can thus be decomposed into a normal component v_y [$m.s^{-1}$] and tangential component v_x [$m.s^{-1}$], as shown in Fig. X-17(a) [Cao 2014]. As the abrasive particles impact the surface with an approach angle α, their normal component of velocity v_y is responsible for penetration of the workpiece material, which leads to deformation wear. The horizontal component of velocity v_x is responsible for cutting action of the particles. In the cutting process, two scenarios are possible: cutting type I in which the particle loses all its kinetic energy during the collision, and cutting type II in which the particle loses only a fraction of its kinetic energy and bounces off the surface.

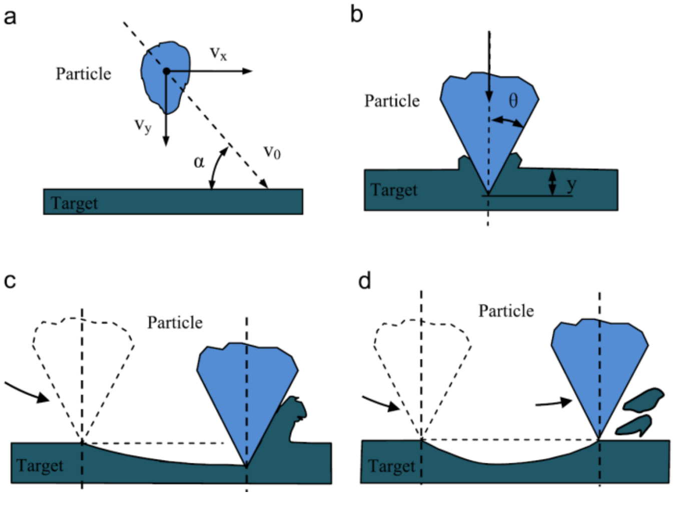

Fig. X-17. Erosion behavior of abrasive particles in MFJP: (a) impact (b) deformation wear (c) material cutting type I (d) material cutting type II [Cao 2014].

Assuming an abrasive hardness greater than that of the workpiece material, in which case deformation of the impacting particles may be neglected, the abrasives are modelled as cones of semi-angle θ hitting the surface with their cone axis perpendicular to the surface. As the cone indents the surface with an increasing depth *d* [mm], its cross sectional area of indentation A_n [mm^2] can be expressed as:

$$A_n = \pi d^2 tan^2\theta \tag{9}$$

The normal component of the equation of motion for abrasive particles, as they progressively indent the workpiece material, can then be written as:

$$m_p \frac{\partial v_n}{\partial t} = P_n A_n \tag{10}$$

where P_n [Pa] is the normal component of plastic flow pressure acting over the area A_n, v_n [mm.s^{-1}] the normal velocity of the particle at a time *t* [s], and m_p [kg] is the mass of the abrasive particle. This equation can be solved under the initial condition $v_n(0) = v_y$ when the particle first contacts the surface, and $v_n(T) = 0$ when the particle fully indents the surface with a depth d_i, leading to an expression for the volume of indentation V_i [mm^3] when reaching the maximum indentation d_i [mm]:

$$V_i = \int_0^{d_i} A_n \, \partial y = \frac{m_p {v_y}^2}{2P_n} \tag{11}$$

The material displaced by indentation is associated with several phenomena: elastic deformation, plastic deformation, or wear removal as debris. However, owing to the low kinetic energy of abrasive particles in MFJP, the direct removal of material due to indentation induced wear is usually negligible (except for brittle mode processing cases, see section X.3.4). This is confirmed by the noticeable absence of material removal at the center of the stagnation area, where particle trajectories are mostly normal to the surface.

Therefore, the main material removal mechanism in MFJP is ductile cutting of the surface under the lateral motion of the penetrating abrasives. Owing to spring back of the material from the elastic component of deformation, the volume of ductile material removal by the indenting abrasives can be expressed as a fraction of the integral along the cutting length *L* [mm] of the cross-section area of the engagement by abrasive particles A_t [mm^2], in the plane perpendicular to the direction of cutting:

$$V \propto \int_0^L A_t \, \partial x \tag{12}$$

The tangential component of force F_t experienced by the abrasive particle is proportional to the tangential component of the workpiece material plastic flow pressure P_t [Pa], applied against the cross-section area A_t, leading to the expression:

$$F_t \propto P_t A_t^b \tag{13}$$

where b ($0.5 \leq b \leq 1$) a material dependent exponent of the cross-section area. The energy equation of the particle can then be solved for the initial condition $v_t(0) = v_x$, and $v_t(T) = v_{out}$ reflecting the probability that a particle may escape the cutting zone with some residual tangential velocity v_{out} (cutting type II):

$$\int_0^L F_t \, \partial x \propto \frac{1}{2} m_p ({v_x}^2 - {v_{out}}^2) \tag{14}$$

By combining eq. 12 – 14, and substituting cV_x ($c \leq 1$) in place of V_{out} (c is the fraction of initial particle velocity on impact), the expression of the volume V [mm^3] of material removed by a single particle can be simplified to a function of its normal and tangential impact velocities as follows:

$$V(v_x, v_y) = k\left(\frac{1}{2}m_\mathrm{p}v_\mathrm{x}^2\right)\left(\frac{1}{2}m_\mathrm{p}v_\mathrm{y}^2\right)^{\frac{2(1-b)}{3}} \tag{15}$$

where k is a coefficient that depends on the workpiece material (compounding contributions from the plastic flow pressure and material spring back), and which requires experimental calibration. The overall material removal rate E [mm^3.s^{-1}] can finally be estimated by taking into account the rate of particles $\sigma_A(r)$ [mm^{-2}.s^{-1}] impacting a specific area of the workpiece surface, as follows:

$$E(r) = \sigma_a(r)V(v_x(r), v_y(r)) \tag{16}$$

Some comparisons of removal depth distribution computed by simulations and measured in experiments are shown in Fig. X-18. In the case of small abrasive particles with a diameter below 1 µm, the single particle impact model generally provides accurate estimates. However, as the particle size further increases, the removal footprint measured in experiments widens noticeably, due to further removal of material caused by secondary impacts of the abrasive particles. The influence of secondary impacts can be reflected by further tracing the particle trajectories to characterize the secondary impact distribution $\sigma'_A(r)$ and velocities $v'_x(r)$, $v'_y(r)$. The predictions from secondary impact models agree more closely with measured data in the case of abrasive particles with diameter above 1 µm (Katsuura 2018).

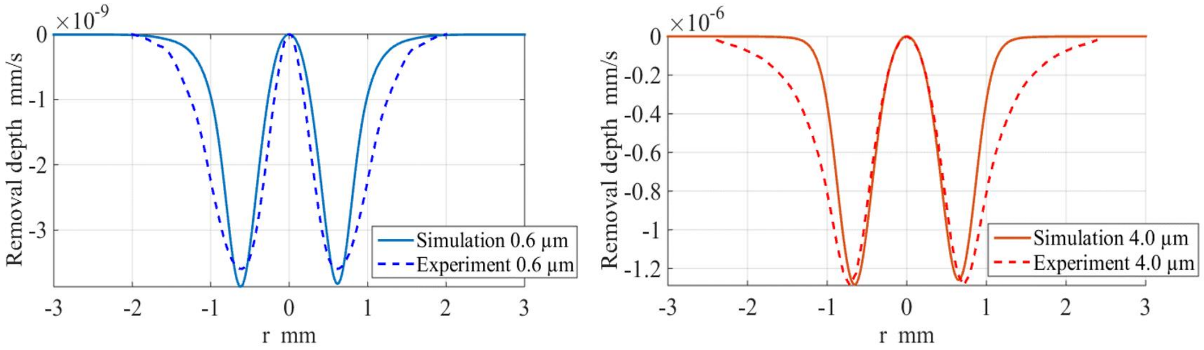

(a) 0.6 µm diameter abrasive particles (b) 4.0 µm diameter abrasive particles

Fig. X-18. Comparison of material removal footprints predicted by single particle impact model and measured experimentally [Katsuura 2018]

X.3.4 Surface Integrity of Hard and Brittle Materials

When processing hard and brittle materials, the potential occurrence of deformation wear on the workpiece by particle impacts should be given special attention. According to Bifano (1991), there exists a critical indentation depth d_c of the abrasive particles, above which brittle fracture of the workpiece surface is expected to occur during machining. d_c [mm] can be expressed as a function of measurable material properties as follows:

$$d_c = 0.15\left(\frac{E}{H}\right)\left(\frac{K_c}{H}\right)^2 \tag{17}$$

where E is the elastic modulus of the material, H the Vickers hardness, and K_c the fracture toughness. The validity of the coefficient 0.15 was verified for several ceramic materials including fused silica, Zerodur and silicon carbide. It corresponds to an arbitrary 10 percent fracturing of the cut walls. Table X-3 shows a summary of these material properties for silicon carbide and tungsten carbide, together with the resulting value for critical depth of indentation.

Table X-3. Material properties of binderless carbide materials used in optical mold fabrication

Material properties	**Silicon carbide**	**Tungsten carbide**
Elastic modulus (E)	410 [GPa]	715 [GPa]
Fracture toughness (K_c)	4.6 [MPa.m$^{1/2}$]	4.8 [MPa.m$^{1/2}$]
Vickers hardness (H)	2800 [Kg.mm^{-2}]	2350 [Kg.mm^{-2}]
Critical depth of indentation	59 [nm]	190 [nm]

Given that the equivalent indentation depth d_i in MFJP can be expressed as function of process and material parameters, it is possible to use the critical indentation depth model to predict the approximate appearance of brittle damage on the workpiece surface, through the relationship $d_i > d_c$. By integration of eq. 11, an expression of d_i is obtained as follows:

$$d_i = \left(\frac{3m_p {v_y}^2}{2\pi P_n \tan^2\theta}\right)^{\frac{1}{3}} \tag{18}$$

Fig. X-19 shows a typical example of brittle material (binderless tungsten carbide) machined by MFJP, with the equivalent indentation depth d_i above (a) and below (b) the critical indentation depth d_c of the processed material. The impact on surface integrity is very clearly observable, with extensive pitting of the brittle mode machined surface versus smoothness of the ductile mode machined surface.

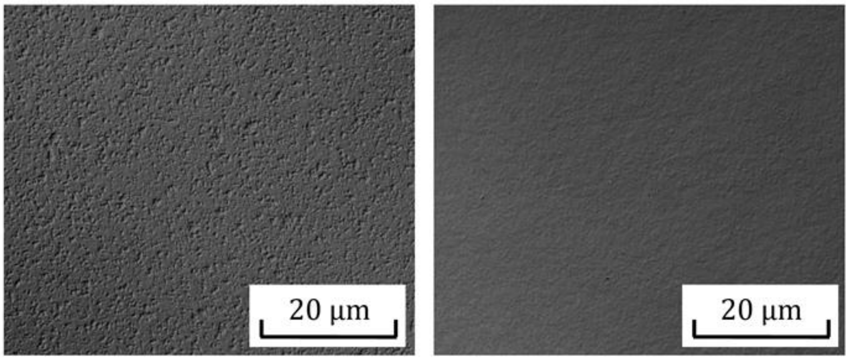

(a) Brittle mode processing ($d_i > d_c$) (b) Ductile mode processing ($d_i < d_c$)

Fig. X-19. Surface integrity of binderless tungsten carbide processed by MFJP [Beaucamp 2014]

X.4 Deterministic Finishing by MFJP

An exploitable characteristic of MFJP is the time dependent nature of material removal during processing. As such, the removal depth per unit of area is a factor of the equivalent time spent by the MFJP beam at a given location on the workpiece. This property can be harnessed to perform deterministic finishing of surfaces, in which the shape accuracy of a workpiece is improved through iterative processing by MFJP. This processing strategy is based on convolution of influence function (material removal footprint) data with tool path information to predict the outcome of a polishing run. The basic principles of deterministic finishing by MFJP are presented in the following sections.

X.4.1 Influence Function

While basic process simulations provide useful indicators of the extent and rate of material removal in MFJP, deterministic finishing usually requires very precise measurements of experimental influence functions. These are generated by impinging a static location on a sacrificial workpiece for a specific amount of dwell time. Fig. X-20 shows an example of such influence function spots generated on a piece of electroless nickel with a slurry of aluminum oxide at a concentration of 20 g.L^{-1}, pressurized at 0.8, 1.2, and 1.6 MPa (from left to right). The 10 s dwell time resulted in a maximum depth of 10 nm at 0.8 Mpa, and 40 nm at 1.6 MPa, as well as a slight variation in the extend of the footprint due to the varying degree of secondary impacting by the abrasive particles (see section X.3.3).

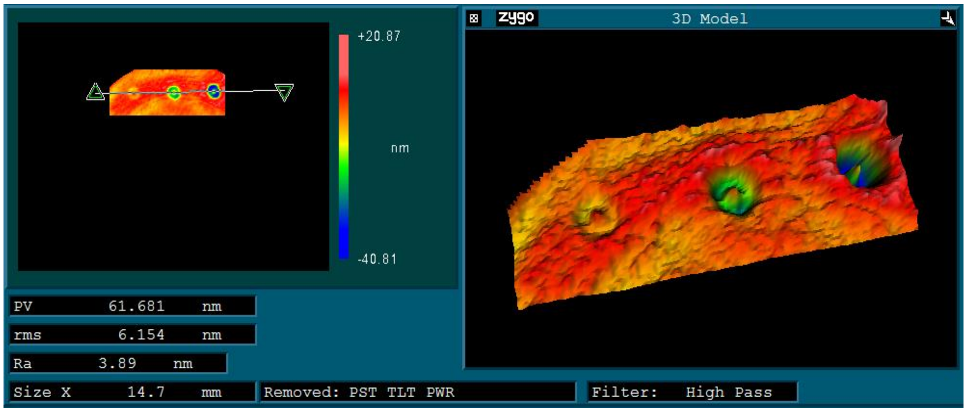

PV 61.681 nm
rms 6.154 nm
Ra 3.89 nm
Size X 14.7 mm
Removed: PST TLT PWR
Filter: High Pass

Fig. X-20. Influence function spots generated on electroless nickel by 0.8, 1.2 and 1.6 MPa MFJP

A continuous model of the footprint shape, as function of the various process parameters such as the nozzle stand-off distance and inlet pressure, can be assembled using a mathematical object called multi-variate spline. The concept consists of associating a N dimensional process parameters space (denoted as u,v,…) with a Cartesian representation space (denoted as x,y,z) of the influence function. Based on a set of measured data (fixed points in the process parameters space, associated with 3D measurements of the influence function), a multivariate spline of the influence function *IF* can be constructed by the tensor product method resulting in the form:

$$IF(p_u, p_v) = \sum_{u=1}^{U} \sum_{v=1}^{V} B_{u,k}(p_u)\, B_{v,l}(p_v)\, A_{u,v} \tag{19}$$

where $B_{u,k}$ and $B_{v,l}$ are univariate B-splines or order k and l respectively, and $A_{u,v}$ are coupling coefficients. This definition can be extended to any number of dimensions in the process parameter space, and the output provides a continuous morphing of the influence function shape between the experimentally collected data points.

X.4.2 Forward Problem

Processing a workpiece by deterministic MFJP usually involves rastering or spiraling the surface, with a track spacing that is a fraction of the influence function spot extent. Typical track spacing of between 5 – 10% of the spot extent is used to attenuate the appearance of cusping across the workpiece surface.

For numerical convenience, the continuous tool path may be discretized into a series of points $\{i \mid 0 \le i \le n\}$ as illustrated in Fig. X-21. The MFJP beam dwells at each point for an equivalent time that is relative to the distance between points in the series, and inverse to the feed of displacement of the beam across the surface. Inlet pressure and nozzle stand-off distance may vary along this tool path, such that the process parameters may be expressed as function of i: $p_u(i)$, $p_v(i)$, …

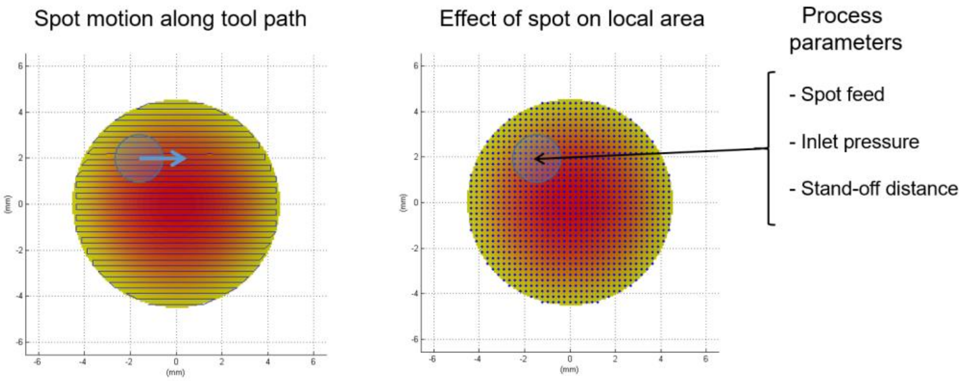

Fig. X-21. Discretization of continuous tool path into dwell points visited by the MFJP influence function

The compound removal of material *CR* by the tool path (usually referred to as the forward problem), can be expressed as a discreet sum of the influence function's multivariate spline and dwell time map *DT*:

$$CR(p_u, p_v) = \sum_{i=0}^{n} DT(i)\, IF(p_u(i), p_v(i)) \tag{20}$$

While *CR* accounts for the material removal profile across the entire workpiece surface, individual points of the tool path vector only affect a localized area of the entire surface matrix.

X.4.3 Inverse Problem

The main attraction of deterministic finishing by MFJP lies in the ability to iteratively improve form accuracy, through repeated measurement and processing of a workpiece. The objective function in this type of processing consists of minimizing the deviation between a target removal profile *TR*, and the predicted compound removal profile *CR*:

$$f(p_u, p_v) = \sqrt{TR - CR(p_u, p_v)} \tag{21}$$

The scale of this numerical problem is vast: the process parameters p_u, p_v, … may vary across the entire series of tool path points, which makes this a numerical optimization problem with n^p input variables. In order to reduce the complexity of this problem, a typical approach consists of selecting initially constant values of the process parameters, and treating the influence function as a point spread function [Fang 2006]. This permits initial assessment of the problem by deconvolution over the time domain, whereby:

$$DT * IF = CR \tag{22}$$

Limitations of the deconvolution method include the requirement for a non-varying influence function, and the tool path covering a rectilinear grid. Thus, this method is used to compute an approximate solution, which can then be used as seed to a more advanced numerical optimization algorithm (such as evolutionary or Newtonian search).

An example of deterministic finishing by the inverse problem solving method is shown in Fig. X-22: an electroless nickel plated aspheric molding die was generated by diamond turning to a form accuracy of 387 nm P-V. Through iterative measuring with a Fizeau interferometer and processing by deterministic MFJP, the form accuracy was improved down to 47 nm P-V. It is noteworthy that the process loop was realized on a standard polishing CNC machine, only capable of positioning with micron level accuracy.

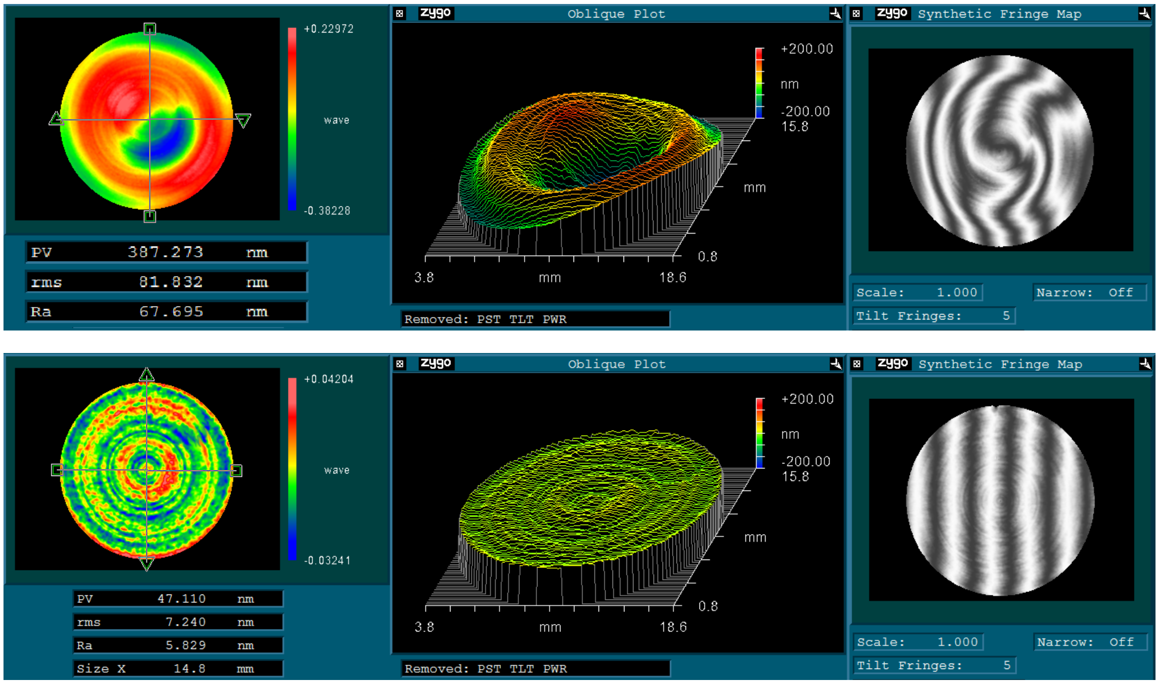

PV 387.273 nm
rms 81.832 nm
Ra 67.695 nm
Removed: PST TLT PWR
Scale: 1.000
Narrow: Off
Tilt Fringes: 5

PV 47.110 nm
rms 7.240 nm
Ra 5.829 nm
Size X 14.8 mm
Removed: PST TLT PWR
Scale: 1.000
Narrow: Off
Tilt Fringes: 5

Fig. X-22. Deterministic finishing of electroless nickel plated aspheric molding die by MFJP.

X.5 MFJP Process Enhancements

As discussed in section X.2.3, there exists in MFJP a strong correlation between abrasive size and inlet pressure on the one hand, and removal rate on the other (Fig. X-9). But increasing these factors in order to enhance material removal rate also leads to an increase in the normal component of velocity and potential degradation of the surface integrity (see section X.3.4). Thus, the MFJP process is usually constrained to lower material removal rates, and its scope for application was initially limited to finishing of near-perfect shape optical surfaces. However, a number of process enhancements have been proposed in order to increase the material removal rate, ranging from the injection of air bubbles to using arrays of nozzles. A number of these enhancements are discussed in this section.

X.5.1 Submerged MFJP

Submerged MFJP is a process variant in which the workpiece is plunged within a tank of circulating slurry, and the nozzle outlet is kept below the waterline of the tank, as shown in Fig. X-23. Experimental data shows that material removal footprints generated in this operation method have a Gaussian-like appearance, instead of the W-shape common in standard MFJP. According to computational fluid simulations, the outflow of slurry from the nozzle outlet has to overcome greater resistance from surrounding slurry, than is the case in standard MFJP in which air is displaced. Accordingly, the tangential speed of the fluid along the workpiece surface is reduced and abrasive particles rapidly lose their kinetic energy, the further away they travel from the center of the impingement region.

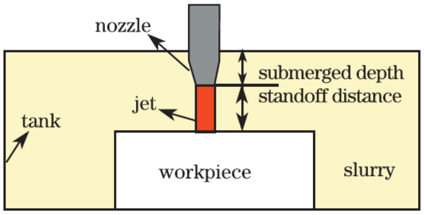

Fig. X-23. Principle of submerged MFJP, in which the nozzle outlet is plunged within a tank of enveloping slurry [Shi 2011]

Material removal rate in submerged MFJP is somewhat lower than the standard process, with removal rate quickly tapering off as the standoff distance increases to more than 10 mm away from the workpiece surface. However, there are distinct advantages in submerged MFJP such as the Gaussian shape of influence functions, which performs better than a W-shape when using the process for deterministic finishing, and surface roughness that is around 50% lower than the standard process (all other parameters being equal). This improvement in surface roughness is understood to arise from the reduced likelihood of air bubbles becoming trapped within the jet plume as it travels through surrounding slurry, as such air bubble can energize the impact of individual abrasives and detrimentally affect the surface.

X.5.2 Air Assisted MFJP

One of the more intensely investigated line of research for the enhancement of material removal rate in MFJP has been the injection of air bubbles into the fluid jet stream, in order to energize the motion of abrasive particles within the carrier fluid. This effect can be achieved either by inclusion of a pulsating mixing valve that admits pressurized air up-front of the nozzle cavity [Messelink 2005], or through the implementation of a special nozzle inside which slurry is drawn into an air stream by Venturi effect [Loc 2013], an example of the latter being shown in Fig. X-24.

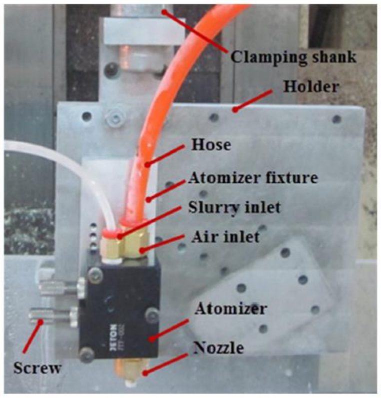

Fig. X-24. Experimental setup of Venturi effect based air-driven MFJP system [Loc 2013]

In the case of both setups, material removal rate was found to greatly increase when compared to standard FJP (more than 1000%). However, the barely controllable mixing of slurry and air also has some side effects, such as a significant break-up of the jet plume at the nozzle outlet, and rapid wear of the nozzle outlet walls. The resulting loss of process stability leads to large fluctuations of the removal rate, and severe degradation of the surface roughness (more than 10,000%). For these reasons, air assisted MFJP may qualify as a micro-blasting rather than micro-polishing process.

X.5.3 Ultrasonic Cavitation Assisted MFJP

Ultrasonic cavitation assisted MFJP is an enhancement in which micro-bubbles are generated directly within the nozzle, with the help of an acoustic transducer located at the back of the cavity. The main advantage of this method lies in the fact that both the size and number of micro-bubbles are controllable through the output frequency f [Hz] and power P [W] of the ultrasonic transducer. Fig. X-25 shows a typical implementation in which an acoustic lens is attached to the transducer [Beaucamp 2017], such that pressure waves may be focused directly upstream of the nozzle outlet. Typical focal length value of the acoustic lens is 50 mm, with the nozzle cavity assuming a cone shape that matches the transducer diameter and focal length.

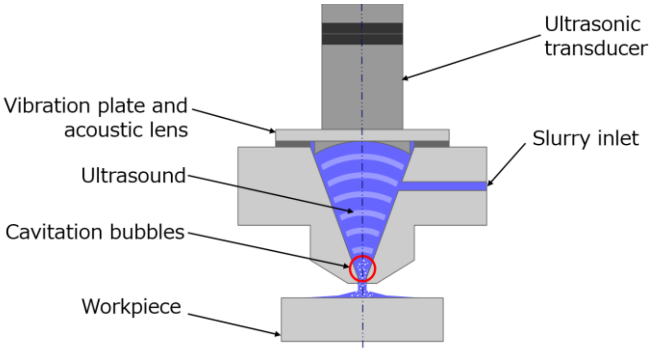

Fig. X-25. Principle of ultrasonic cavitation assisted MFJP [Beaucamp 2017]

Typical operating frequency of the ultrasonic transducer is in the range 26 - 130 kHz, and the output power in the range 50 - 400 W. The high intensity of the focused beam maximizes generation of cavitation bubbles, while proximity of the generation region to the nozzle outlet ensures delivery of micro-bubbles to the workpiece surface in the shortest time possible. The lifetime of micro-bubbles is measured in cycles of the acoustic waves, with a value of around 200 cycles typically observed in basic experiments. Table X-4 shows the expected lifespan of cavitation micro-bubbles, as a function of the ultrasonic generation frequency. Accordingly, micro-bubbles should pass though the nozzle outlet and reach the workpiece within a few milliseconds. Integration of the path time through fluid stream computed numerically dictates that nozzle stand-off distance should be no more than a few centimeters. This constraint can thus restrict applicability of ultrasonic cavitation assisted systems in cases where recessed areas of a workpiece are more than a few centimeters deep.

Table X-4. Lifespan of micro-bubbles generated by ultrasonic cavitation (based on 200 cycles)

Transducer Frequency	26 kHz	78 kHz	130 kHz
Micro-bubble lifespan	7.2 ms	2.4 ms	1.4 ms

Material removal rate increase of up-to 380% compared to standard MFJP has been observed, when processing metals and glass by ultrasonic cavitation assisted MFJP. Fig. X-26(a) shows that removal rate increases almost linearly as a function of ultrasonic output (ultrasonic frequency has a weaker impact on removal rate variation, the power output being equal). Crucially, surface roughness can be maintained or even slightly improved as shown in Fig. X-26(b). Thus, while the overall material removal rate boost of ultrasonic cavitation assisted MFJP is lower than that of air-assisted systems, the maintaining of surface roughness is a considerable advantage.

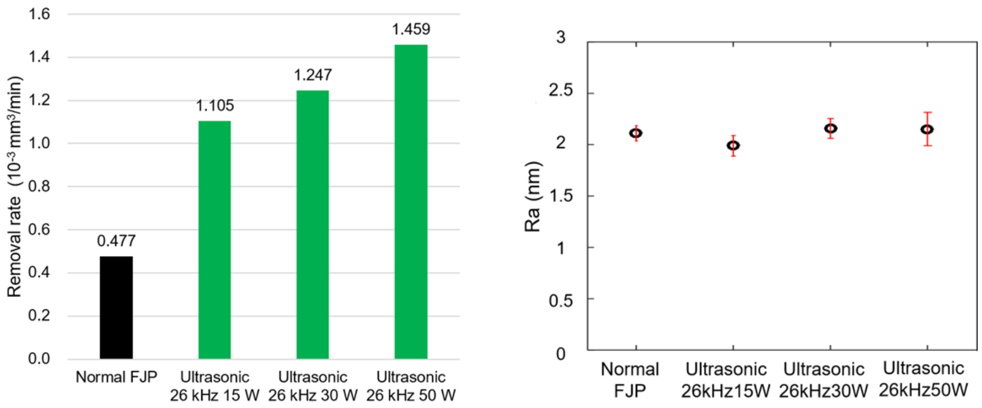

(a) Material removal rate (b) Surface roughness

Fig. X-26. Comparison between standard and ultrasonic cavitation assisted MFJP processing of BK7 optical glass [Beaucamp 2017]

X.5.4 Non-Newtonian Fluid Assisted MFJP

Fluids containing a dilute solution of long-chain polymers, such as polyacrylamide (PAM) and polyethylene oxide (PEO), are often described as non-Newtonian. Their viscosity and resistance to external deformation (elasticity) are dependent on the shear-rate and shear-rate history of the fluid, with the fluid viscosity typically increasing as the shear-rate increases. When using a non-Newtonian carrier fluid for MFJP processing, the shear thickening effect is most noticeable in the near wall region of the impinging jet, where a stagnation layer appears whenever an abrasive particle attempts to punch through the fluid and reach the workpiece surface, as shown in Fig. X-28 [Kowsari 2014]. The extra drag experienced by the abrasive particles softens their impact on the surface, causing a noticeable reduction of the overall material removal rate. However, the possibility of increasing the elasticity of non-Newtonian fluids independently from their viscosity brings useful benefits, such as decreased jet plume instability (break-up), and improved focusing of the beam. In experimental tests, the width of channels machined with non-Newtonian fluids could be reduced by about 20% as compared to water based MFJP (all other parameters being equal).

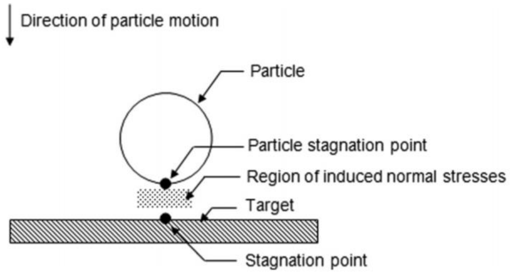

Fig. X-28. Extra drag experienced by abrasive particles near the workpiece surface, due to normal stress induced stagnation [Kowsari 2014]

X.5.5 Magnetorheological Fluid Assisted MFJP

Magnetorheological (MR) fluids are a type of carrier fluid that can greatly increase its apparent viscosity when subjected to an external magnetic field. MR fluids are typically loaded with micrometer scale ferromagnetic particles, which under the influence of a magnetic field align themselves into lines of magnetic flux. In MR fluid assisted MFJP, the jet plume is stabilized and stiffened by an axial magnetic field generated with the help of an electromagnet. This method has been shown to prevent breakup of the jet plume has the dense MR fluid exits the nozzle outlet [Tricard 2006], as shown in Fig. X-29. The stabilization persists for up-to several meters, allowing for precise targeting of remote and difficult to access workpiece areas. Some advantages of this method include higher removal rate due to the increased apparent viscosity, while maintaining nanometer scale surface roughness, although the handling and recycling of MR fluid requires highly specialized equipment and knowledge, which makes the implementation of a MR fluid assisted MFJP setup somewhat challenging.

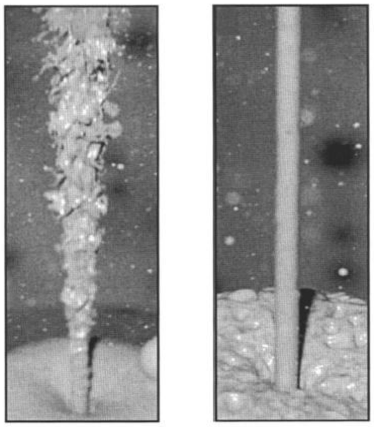

MR Fluid
Magnet Off

MR Fluid
Magnet On

Fig. X-29. Influence of magnetic field on the shape of a magnetorheological fluid jet beam [Tricard 2006]

X.5.6 Nozzle Array MFJP

Precision artifacts made of repeating elements, such as the micro-lens arrays used in fiber optic end-connectors to telecommunications terminals (as well as replication molds for such artifacts), are well suited for parallelized processing by arrays of MFJP nozzles. As shown in Fig. X-30, the array of nozzles may either match exactly the grid of micro-lenses, or span a subset of the entire distribution [Wang 2017]. While basic implementations of the process may amount to the straight forward drilling of nozzle outlets into a base plate made of stainless steel, performance of nozzle array systems in terms of removal rate uniformity usually compare unfavorably against single nozzle MFJP. The lower precision of conventionally drilled metal nozzles is one factor, which can be remediated by laser drilling of a large sapphire insert.

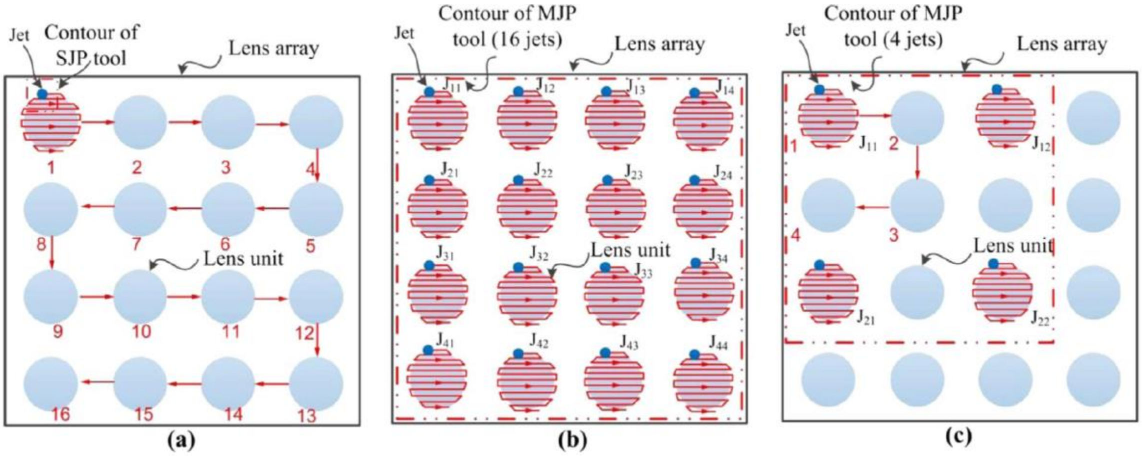

Fig. X-30. Principle of lens array polishing with (a) single MFJP nozzle, (b) 4 x 4 array of nozzles, and (c) 2 x 2 array of nozzles [Wang 2017]

A less tractable factor is interference between impinging MFJP beams, as shown in Fig. X-31. As the carrier fluid attempts to move across the workpiece surface and away from the impingement zone, interference in the fluid flow causes large variations in the maximum depth of material removal of beams issuing from the center and edge of the nozzle array, as well as the appearance of material removal interference patterns in between individual influence function spots. Reduction of these interference issues requires a minimum spacing between beams of several times the beam width, which makes the subset processing strategy shown in Fig. X-30(c) the most practical.

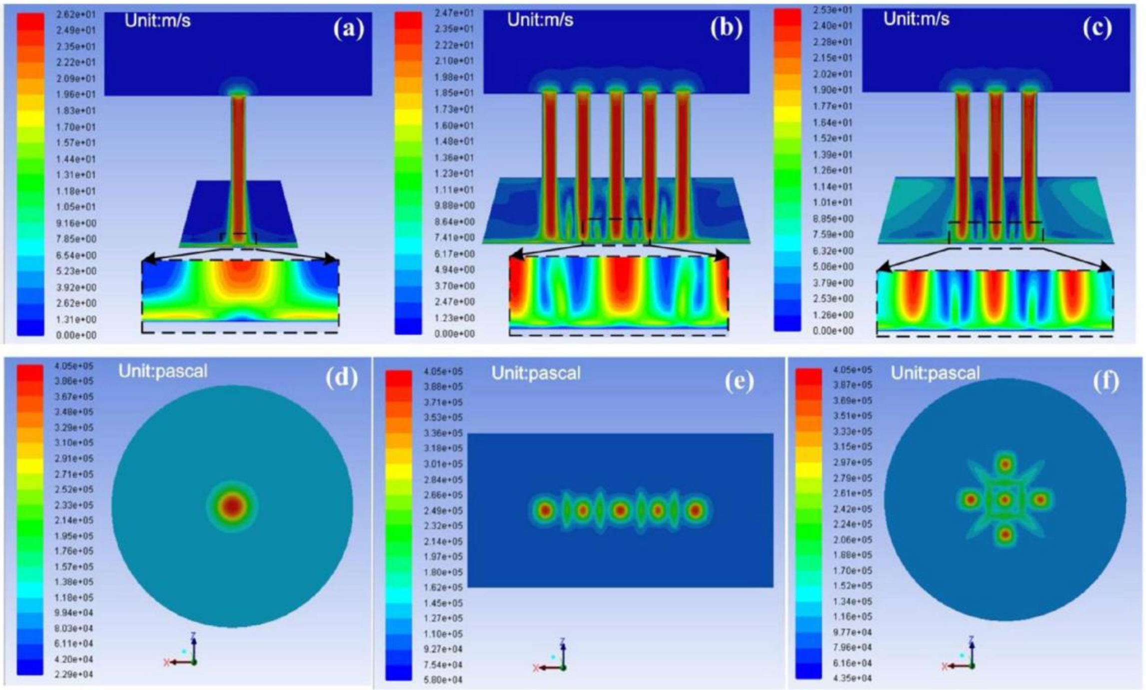

Fig. X-31. Computational fluid simulation demonstrating MFJP beam interference in linear and radial arrangements of nozzle outlets [Wang 2017]

X.5.7 Rotary Multi MFJP

Combining several MFJP beams into a single influence function spot, from radially distributed inclined attack directions around a single impact zone, is another method that has been explored in order to enhance the material removal rate of the process. Fig. X-32 shows the design of a rotary multi-nozzle MFJP head, which offers the added benefit of suppressing directionality of the combined influence function spot [Shiou 2015]. The head consists of a shank coupled to a rotating shaft, supported by thrust bearings at the top and bottom of a static compartment. The pressurized slurry enters the top part of the cavity, and flows out through a number of nozzle outlets attached to a plate at the bottom of the rotating shaft. Experimental data has found some unique advantages to this method, such as decreased surface roughness as the inlet pressure is increased between 0.4 and 0.8 MPa (a reverse trend to that observed in single jet MFJP). A dependency between surface roughness and angular rotation rate of the shaft was also observed, with an optimum speed of 20 rpm reported in the case of 6 nozzle outlets.

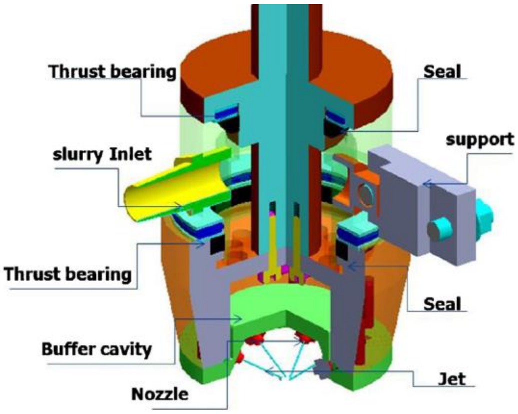

Fig. X-32. Design principle of rotary multi-jet polishing head [Shiou 2015]

Summary and Outlook

In this chapter, Micro Fluid Jet Polishing (MFJP) was introduced as a flexible process for super-fine finishing of small and complex workpiece geometries. The principal advantages of MFJP include lack of tool wear, ease of access to deeply recessed areas, wide range of beam diameter from 0.1 to 1.0 mm, and the ability to reach nanometer-level surface finish on various materials. Comprehensive modelling of the process has been published in the literature, covering all aspects from development of the jet plume to entrainment and impacting of the surface by abrasive particles. By application of these mathematical models, material removal rate in MFJP is eminently predictable and controllable, allowing for ultra-precise applications such as deterministic finishing and functional surface generation with nanometer-scale height resolution.

Some drawbacks have been highlighted, such as the potential occurrence of surface contamination by abrasives, which can be mitigated by increasing the particle size and decreasing the operating pressure, as well as the generally low material removal rate of the standard MFJP process. However, a number of enhancements can boost the material removal rate, such as air-assisted, ultrasonic cavitation assisted, and multiple beam MFJP, while other enhancements such as submerged polishing and non-Newtonian carried fluids can improve the achievable surface roughness.

Present limitations of MFJP include the minimum beam diameter achievable of 0.1 mm, due to the difficulty of drilling narrow holes in sapphire. It is however expected that advances in laser drilling and electro-discharge machining will allow for smaller nozzle diameter in the near future, and permit smaller lateral feature size in functional surface generation. Another area for future improvement is expected in the use of finer nanoscale abrasives, in conjunction with the enhanced air-driven and ultrasonic systems. It is conceivable that surface machining on par with ultra-fine processes such as ion beam figuring, may be possible with nanoparticle-loaded slurries.

References

O. Fähnle, H. van Brug, H. Frankena, Fluid jet polishing of optical surfaces, Applied Optics 37, pp. 6771 - 6773 (1998)

T. Matsumura, T. Muramatsu, S. Fueki, Abrasive water jet machining of glass with stagnation effect, CIRP Annals Manufacturing Technology, Vol. 60, No. 1, pp. 355 - 358 (2011)

A. Beaucamp, Y. Namba, Super-smooth finishing of diamond turned hard X-ray molding dies by combined fluid jet and bonnet polishing, CIRP Annals Manufacturing Technology, Vol. 62, No. 1, pp. 315 - 318 (2013)

Z. Cao, C. Cheung, M. Ren, Modelling and characterization of surface generation in Fluid Jet Polishing, Precision Engineering, Vol. 43, pp. 406 - 417 (2016)

S. Booij, Fluid Jet Polishing: possibilities and limitations of new fabrication technique, Ph.D. Thesis, Technische Universiteit Delft (2003)

Z. Menter, Two-Equation Eddy-Viscosity Turbulence Models for Engineering Applications, American Institute of Aeronautics and Astronautics Journal, Vol. 32, No. 8, pp. 1598 – 1605 (1994)

A. Beaucamp, Y. Namba, R. Freeman, Dynamic Multiphase Modeling and Optimization of Fluid Jet Polishing Process, CIRP Annals Manufacturing Technology, Vol. 61, No. 1, pp. 315 – 318 (2012)

P. Guo, H. Fang, J. Yu, Edge effect in fluid jet polishing, Applied optics, Vol. 45, No. 26, pp. 6729 – 6735 (2006)

R. Wäger, W. Messelink, H. Looser, O. Fähnle, K. Heiniger, Particle tracking in a fluid jet polishing slurry flow, SPIE Conference Optifab, Rochester (2005)

Z. Cao ,B. Cheung, Theoretical modelling and analysis of the material removal characteristics in fluid jet polishing, International Journal of Mechanical Sciences, pp. 89158 - 166 (2014)

C. Huang, S. Chiovelli, P. Minev, J. Luo, K. Nandakumar, A comprehensive phenomenological model for erosion of materials in jet flow, Powder Technology, Vol. 187, No. 3, pp. 273 - 279 (2008)

T. Katsuura, Characterization of process and mechanism in ultrasonic cavitation assisted fluid jet polishing, Master Dissertation, Kyoto University (2018).

T. Bifano, T. Dow, R. Scattergood, Ductile-regime grinding: a new technology for machining brittle materials, Transactions of ASME, Vol. 113, pp. 184 – 189 (1991)

A. Beaucamp, Y. Namba, W. Messelink, D. Walker, P. Charlton, R. Freeman, Surface integrity of fluid jet polished tungsten carbide, Procedia CIRP, Vol. 13, pp. 377 – 381 (2014)

H. Fang, P. Guo, J. Yu, Dwell function algorithm in fluid jet polishing, Applied Optics, Vol. 45, No. 18, pp. 4291 – 4296 (2006)

C. Shi, J. Yuan, F. Wu, Y. Wan, Ultra-precision figuring using submerged jet polishing, Chinese Optics Letters, Vol. 9, No. 9, pp. 092201 (2011)

W. Messelink, R. Waeger, T. Wons, M. Meeder, K. Heiniger, O. Faehnle, Prepolishing and finishing of optical surfaces using fluid jet polishing, Optical Manufacturing and Testing VI, International Society for Optics and Photonics, Vol. 5869, pp. 586908 (2005)

P. Loc, F. Shiou, Z. Yu, H. Hsu, Investigation of Optimal Air-Driving Fluid Jet Polishing Parameters for the Surface Finish of N-BK7 Optical Glass, Journal of Manufacturing Science and Engineering, Vol. 135, No. 1, pp. 011015 (2013)

A. Beaucamp, T. Katsuura, Z. Kawara, A novel ultrasonic cavitation assisted fluid jet polishing system, CIRP Annals Manufacturing Technology, Vol. 66, No. 1, pp. 301 - 304 (2017)

K. Kowsari, D. James, M. Papini, J. Spelt, The effects of dilute polymer solution elasticity and viscosity on abrasive slurry jet micro-machining of glass, Wear, Vol. 309, No. 1, pp. 112 - 119 (2014)

M. Tricard, W. Kordonski, A. Shorey, C. Evans , Magnetorheological Jet Finishing of Conformal, Freeform and Steep Concave Optics, CIRP Annals Manufacturing Technology, Vol. 55, No. 1, pp. 309 – 312 (2006)

C. Wang, C. Cheung, L. Ho, M. Liu, W. Lee, A Novel Multi-jet Polishing Process and Tool for High-efficiency Polishing, International Journal of Machine Tools and Manufacture, Vol. 115, pp. 60 - 73 (2017)

F. Shiou, A. Asmare, Parameters optimization on surface roughness improvement of Zerodur optical glass using an innovative rotary abrasive fluid multi-jet polishing process, Precision Engineering, Vol. 42, pp. 93 - 100 (2015)